Desalination and Water Treatment
www.deswater.com

doi:10.5004/dwt.2020.24884

174 (2020) 400–413
January

Application of NFO-GO composite for the removal of Acid blue 25 toxic dye from aqueous solution

Taznur Ahmed[a,*], Abdul Matin Ali[b], Susmita Sen Gupta[b]

[a]*Department of Chemistry, Science College, Kokrajhar, Pin: 783370, Assam, India, Tel. +91 9435125909; email: ahmed.tazu@gmail.com*
[b]*Department of Chemistry, B N College, Dhubri, Pin: 783327, Assam, India, Tel. +91 7002739569; email: abdulmatinali@gmail.com (A.M. Ali), Tel. +91 7086853035; susmita2101@yahoo.co.in (S.S. Gupta)*

Received 7 February 2019; Accepted 10 September 2019

ABSTRACT

In this work, a facile one-step solvothermal approach to the synthesis of the $NiFe_2O_4$-graphene oxide composite was studied. The material was characterized by the X-ray diffraction, transmission electron microscopy, Brunauer–Emmett–Teller surface area, zeta potential, and thermogravimetric analysis measurement. The prepared material used for the adsorption of Acid blue 25 under various experimental conditions. The initial rapid adsorption of dye species attained an equilibrium within 240 min. The interaction much more close to second-order kinetics with a rate constant 1.41×10^{-3} g mg^{-1} min^{-1}. The Langmuir monolayer capacity of the interaction was 104.16 mg g^{-1}. The interaction was endothermic with ΔH 64.319 kJ mol^{-1} accompanied by a rise in entropy and a decrease in Gibb's free energy. Moreover, the activation energy (4.87 kJ mol^{-1}) indicated the adsorption process might be physically controlled.

Keywords: Graphene oxide; Nanocomposite; Adsorption; Langmuir isotherm; Kinetics; Acid blue

1. Introduction

Water is the most precious and indispensable natural resource on earth. Rapid industrialization and various human activities have been responsible for continuously contaminating water by adding different biodegradable and non-biodegradable, persistent, hazardous and toxic pollutants. Water is particularly vulnerable to contamination from the discharge of wastewaters by various industries. These toxic substances as contaminants enter into the food chain have intensified threatening deteriorations towards human health and living organism. Some of the pollutants such as dyes and pigments release to the water sources by textile, dyeing, printing ink, leather, and other related industries. Among the known pollutants are dyes of various classes that not only affecting aesthetics merits but also reducing light penetration and photosynthesis in addition to carcinogenic effects. Azo dye even in small amounts causes damage to aquatic biota or humans by mutagenic and it is also carcinogenic.

Among the different available treatment, adsorption technology draws much attention towards research due to its merits of effectiveness, efficiency, and economy [1]. Adsorption is a surface phenomenon, which arises due to interactions between the individual atoms, ions or molecules of an adsorbate and those present in the adsorbents surfaces. The process involves an array of phenomena that can alter the distribution of pollutants among the constituent phases and interfaces of the subsurface system, and convey the separation of a substance from one phase accompanied by its accumulation at the surface of another [2]. Various conventional and non-conventional adsorbents are used to remove different water pollutants. A few of them are zeolites [3], clay and clay minerals [4,5], inorganic oxides [6], etc. However, all these adsorbents have some disadvantages

* Corresponding author.

1944-3994/1944-3986 © 2020 Desalination Publications. All rights reserved.

either in adsorption capacities or inconvenience in the separation of the materials after loaded with the pollutants. Therefore, efforts are still needed to get the new promising adsorbent.

During the last few years, one form of carbon, namely, Graphene and its derivatives have acquired great interest as an adsorbent to treat wastewater. Graphene (GN), a two-dimensional material (2D), composed of a layer of carbon atoms packed into a honey network, long-range π-conjugation in graphene yields remarkable and unique properties, more important here is its theoretical surface area (2,630 $m^2 g^{-1}$) [7]. All these properties support graphene (GN) as an ideal building block in nano-composites. The high surface area of graphene improves interfacial contact with the other components. Furthermore, the large surface area of GN prevents the aggregation of secondary components, so that some unique properties in the nanoscale can be preserved [8]. The graphene and its metal oxide composites have been explored as adsorbents for the removal of pollutants [9,10]. Along with graphene, graphene oxide (GO) (a derivative of GN) has received great interest for the researcher as [11,12] because of its well organized sp^2-hybridized carbon nanostructures and well spread higher specific negatively charged surface area that can be easily prepared from natural graphite by chemical oxidation-exfoliation-reduction procedure [13]. During the chemical oxidation process a huge number of oxygen-containing functional groups associated with the GO [14,15]. This modification on the surface structure made this substrate very ideal to anchor many inorganic nanoparticles for the increment of widespread [16,17].

Ferrite of the type MFe_2O_4 (M = Zn, Co, Mn, Ni, etc.) is magnetic materials with cubic spinel structure that are used in wide technological applications in the past decade [18,19]. $NiFe_2O_4$ is one of the most important spinel ferrites with an inverse spinel structure showing ferrimagnetism that originates from the magnetic moment of the anti-parallel spin of between Fe^{3+} ion at the tetrahedral site and Ni^{2+} ion at the octahedral site [20]. $NiFe_2O_4$ is an interesting magnetic material due to its chemical stability and mechanical hardness. Thus combining the advantage of graphene oxide composites (GOC) with magnetic NFOs particles to fabricate promising noble adsorbents opens a new possibility for the achievements of desirable absorptivity. Additionally, NFO-GO also shows the advantage of low toxicity, low cost, and eco-friendliness.

GO with varying oxygen-containing groups shows enormous adsorption property. Several researchers had reported the application of GO and graphene nano-sheet composite in the adsorption field. Guo et al. [21] investigated the adsorption capacity of GO/polyethylenimine hydrogel for the adsorption of Rhodamine B (RhB) from aqueous solution with the adsorption capacity of 114.41 mg g^{-1} and the process followed the pseudo-second-order kinetics. Wang et al. [22] studied the adsorption of fuchsine from the water on graphene-based magnetic nanocomposite yielded the Langmuir monolayer adsorption capacity of 49.46 mg g^{-1} followed pseudo-second-order kinetic. Tiwari et al. [23] had reported the adsorption capacity of 6.17 and 9.18 mg g^{-1} for Methylene blue and RhB respectively on the reduced GO-based hydrogels and the process preferably followed the Freundlich isotherm. Wang et al. [24] had reported the adsorption capacity of 90, 66, 22, and 67 mg g^{-1} for phenol, catechol, resorcinol, and hydroquinone respectively on graphene aerogels mesoporous silica framework at 25°C with the contact time of 24 h.

However, few researchers were reported to work with graphene-based nanomaterials as an adsorbent for pollutant removal., Lu et al. [25] reviewed a good number of published works where the synthesis and use of various GO-based nanomaterial for the removal of pollutants from the aqueous environment were incorporated. Wang et al. [22] used Fe_3O_4-GO nanocomposite as an adsorbent for the removal of fuchsine from aqueous solution. The use of GO/ZnO composite as a reusable adsorbent for pollutant management was also reported [26]. The synthesis and adsorptive use of super-paramagnetic GO-Fe_3O_4 hybrid composite were reported by Xie et al. [27].

Taking these advantages, the present work tried to understand the absorption mechanism for typical organic dye Acid blue 25 (AB 25) pollutant on the $NiFe_2O_4$-graphene oxide composite (NFO-GOC).

2. Materials and methods

2.1. Materials

Graphite powder, H_2SO_4, H_3PO_4, ethylene glycol (EG), $Fe(NO_3)_3{\cdot}9H_2O$, $Ni(NO_3)_2{\cdot}6H_2O$, NaOH, EtOH, were procured from Mark Chemical Laboratory Reagent Co. Ltd., (Worli, Mumbai) and used without further purification. The AB 25 (Molecular formula: $C_{20}H_{13}N_2NaO_5S$, CI Classification number: 62055) was also procured from Mark Chemical Laboratory Reagent Co. Ltd., (Worli, Mumbai). The structure of AB 25 is given in Fig. 1.

All chemicals used in this study were of commercially available analytical grade.

2.2. Synthesis of adsorbent

2.2.1. Preparation of GO

GO was synthesized by modified Hummers and Offeman process [28,29] in which 1.5 g graphite flakes and 9.0 g $KMnO_4$ were successfully added into a mixture of concentrated H_2SO_4 and concentrated H_3PO_4 of ratio 9:1 by volume under continuous stirring. The mixture stirred for 12 h at 323 K. Finally, the mixture was cooled and poured slowly under vigorous stirring into the ice with 30% of H_2O_2, then the mixture was repeatedly washed with 30% HCl and ethanol and then dried it at 353 K.

2.2.2. Preparation of $NiFe_2O_4$

Nickel ferrite (NFO) was synthesized by following the procedure [30] where 2 mmol of $Ni(NO_3)_2{\cdot}6H_2O$ and 4 mmol of $Fe(NO_3)_3{\cdot}9H_2O$ were dissolved in 50 mL of EG. Separately 16 mmol of NaOH was dissolved in another 50 mL of EG. The solution of NaOH added to the solution of metal nitrate while stirring at room temperature causing an immediate color change. The mixture was stirred for 4 h. After then, a mixture of water and EG (1:10) was added in two equal portions while temperature raises during 1–1.5 h to 473–483 K.

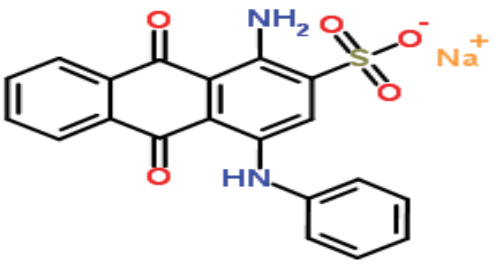

Fig. 1. Structure of AB 25.

Finally, the temperature kept constant for further 1 h. The mixture cooled at room temperature and the precipitate separated and washed several times with methanol. It was then dried and calcined at 823 K. The dark brown powdered obtained as $NiFe_2O_4$.

2.2.3. In situ preparation of NFO-GOC

The prepared GO (0.9 g) was exfoliated by ultrasonication in 80 mL of EG for more than 3 h. 1.72 g of $Fe(NO_3)_3{\cdot}9H_2O$, 0.95 g of $Ni(NO_3)_2{\cdot}6H_2O$ and1.5 g of NaOH then dissolved in GO-EG solution at ambient temperature. After stirring for about 30 min, the solution was transferred into 100 mL Teflon-lined stainless-steel autoclave and kept at 473 K for about 6 h followed by cooling at ambient temperature naturally. The black precipitate centrifuged, washed several times by EtOH and finally dried at 333 K in a vacuum oven.

2.3. Adsorption of dye

The adsorption of dye in aqueous solution on the prepared NFO-GOC was performed in a batch experiment. In the typical process, the adsorbent of the fixed amount was added into 50 mL of dye solution of desired initial concentration and allowed to shake in a thermostated water bath shaker (Superior Scientific Industries, Timber Market, Ambala, Haryana, India, ISO 9001:2008) for a pre-fixed time. At the pre-determined time interval, the solution separated from the mixture by centrifugation. The concentration of dye in the supernatant solutions was measured by a visible spectrometer (Elico Limited SL 177, Hyderabad, Andhra Pradesh). The amount of dye adsorbed per unit mass of adsorbent (q) and the extent of adsorption (%) was calculated by using the mass balanced equation:

$$q = \frac{\left(C_0 - C_e\right)V}{m} \tag{1}$$

$$\text{Extent of adsorption}\left(\%\right) = \left[\frac{\left(C_0 - C_e\right)}{C_0}\right] \times 100 \tag{2}$$

where q was (mg g^{-1}) the amount of adsorbate adsorbed per gram of the adsorbent. C_0 (mg L^{-1}) and C_e (mg L^{-1}) was the initial and equilibrium concentration of dye. V was the volume of the solution taken during an experiment in L and m was mass of the adsorbent in g. The adsorption was studied under various experimental conditions of initial dye concentrations, adsorbent load, interaction time, pH and solution temperature. The different experimental variables are listed in Table 1. The reusability investigation of the adsorbent for its adsorption capacity was carried out after the desorption of loaded adsorbents.

2.4. Characterization of adsorbent

The powdered X-ray diffraction (XRD) measurement was recorded using Bruker AXS (Germany) X-ray powder diffractometer Model D8 by focusing on monochromatized Cu Kα radiation of wavelength 0.15418 nm with a step size of 0.02° (2θ). The specific surface areas, pore diameter and pore volume of NFO-GO composite were determined by Brunauer–Emmett–Teller (BET) N_2 gas methods using automated gas sorption analyzer (Quantachrome® ASiQwin™ Instrument, NOVA-1000 Version 3.70, ANTON PAAR INDIA PVT. LTD., Gurgaon, Haryana, India). The high-resolution transmission electron microgram (HRTEM) image and energy dispersive X-ray (EDX) were obtained by using a JEOL JEM-2100 instrument for the morphological surface (JEOL Ltd., Akishima, Tokyo, Japan). The zeta potential was measured (Zeta sizer, Malvern) to know the nature of charges at the surface. The thermogravimetric analysis (TGA) was carried out to study the thermal stability.

Table 1
Experimental conditions for adsorption study

Sl. No.	Parameter for adsorption process	Experimental set-up
1	Influence of time	Adsorbent 0.1 g L^{-1}, dye concentration 10 mg L^{-1}, pH 6.5, temperature 303 K, time 10–240 min
2	Influence of dye concentration	Adsorbent 0.1 g L^{-1}, pH 6.5, time 240 min, temperature 303 K, dye concentration 10–30 mg L^{-1}
3	Influence of adsorbent load	Dye concentration 10 mg L^{-1}, pH 6.5, temperature 303 K, time 240 min, adsorbent 0.02–0.18 g L^{-1}
4	Influence of pH	Adsorbent 0.1 g L^{-1}, dye concentration 10 mg L^{-1}, temperature 303 K, time 240 min, pH 2.0–11.0
5	Influence of temperature	Adsorbent 0.1 g L^{-1}, dye concentration 10 mg L^{-1}, time 240 min, pH 6.5, temperature 303–333 K

3. Results and discussion

3.1. Adsorbent characterization

3.1.1. XRD analysis

The XRD pattern of $NiFe_2O_4$ and NFO-GOC and GO are shown in Fig. 2. All the detectable peaks were indexed and the data found similar to that for the standard data for the inverse spinel structure of $NiFe_2O_4$ (JCPDS 86-2267) [31]. The NFO-GOC showed a broad peak at a 2θ value of 25.1° corresponding to the interplanar spacing of 0.36 nm. The interplanar spacing (d_{hkl}-value) for the peak located at 30.4°, 35.7°, 39.1°, 43.4°, 53.9°, and 57.4° are 0.29, 0.25, 0.23, 0.20, 0.17 and 0.16 nm corresponding to the planes (220), (311), (222), (400), (422), and (511). The crystals sizes of the NFO-GO composite calculated by using Scherrer equation's ($D_p = 0.94\lambda/(\beta_{1/2}\text{Cos}\theta)$, where λ is the wavelength for the of Cu K_α radiation, θ is the diffraction angle, $\beta_{1/2}$ is full width at half maximum [32] from X-ray line broadening reflection as 11.48, 5.72, 6.99, 7.02, and 12.84 nm, respectively. The average crystal size is 8.74 nm.

3.1.2. High-resolution transmission electron micrograph

The HRTEM analysis of the NFO-GO composite (Fig. 3) indicated that the NFO particle was incorporated within the GO sheets. The particle of various sizes (6.99, 11.4, and 12.8 nm, etc.) were well distributed throughout the GO sheet, which were of a good agreement to that of the particle size calculated from the XRD experiment. The spacing within the lattice fringes in the HRTEM images were 0.17, 0.20, 0.23, 0.25, 0.29, and 0.34 nm which can be assigned to the plane (422), (400), (222), (311), (220) and the spacing of the GO (002) plane. The interplanar spacing (d_{hkl}-value) and the ring pattern are consistent with the XRD data.

3.1.3. EDX analysis

EDX analysis (Fig. 4) confirms the presence of nickel, iron, oxygen, and carbon elements in this nanocomposite.

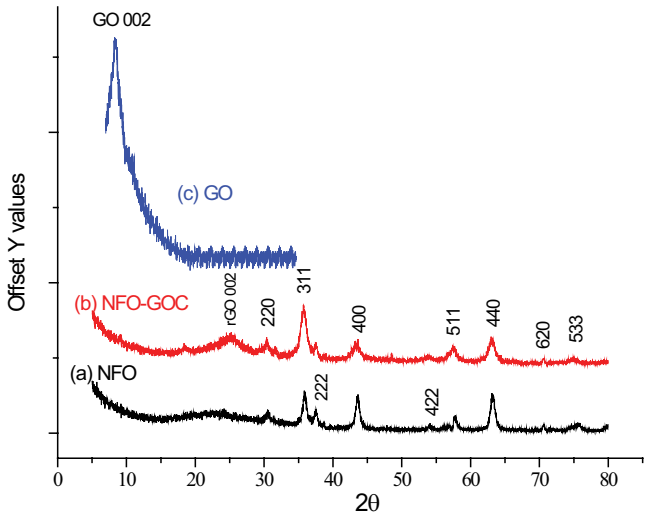

Fig. 2. XRD plots of (a) $NiFe_2O_4$ composite, (b) $NiFe_2O_4$-graphene oxide composite, and (c) graphene oxide.

3.1.4. Surface area determination

The surface area of the adsorbent NFO-GO was determined by BET analysis. The BET analysis for the microstructural parameter of NFO-GO composite was characterized using N_2 adsorption–desorption isotherm (Fig. 5). The isotherm exhibited wider hysteresis loop at high relative pressure indicate type I according to International Union of Pure and Applied Chemistry classification, the feature of the isotherm revealed that the NFO-GO composite present high adsorption performance with narrow slit pores.

The pore size distribution (Fig. 5, inset) showed that the pore size exhibited a very narrow distribution. The composite (NFO-GO) possessed well-developed BET specific surface areas 88.027 $m^2\ g^{-1}$ whereas the specific surface area of GO as reported was 31.4 $m^2\ g^{-1}$ [33], the total pore volume of 0.131 cc g^{-1} and average pore diameter of 3.48 nm calculated from the corresponding nitrogen isotherm.

3.1.5. Zeta potential analysis

The measurement of zeta potential showed that the NFO-GO composite did not possess the zero point charge within the pH range (~5.0 to 9.0) used in the study, indicating the negative surface charge of the adsorbent. The zeta potential values to the pH value are depicted in Fig. 6.

3.1.6. Thermogravimetric analysis

TGA of NFO-GOC showed that a weight loss of ~10% occurred up to 373 K this might be due to loss of water vapors. In the temperature range 373 to 800 K, weight loss of about 23% was observed, which might be due to the oxidation of carbon [34]. The approximate weights of nearly 67% found after oxidation, which related to the weight of NFO-GO. The weight percentages of NFO-GO to temperature plotted in Fig. 7.

3.2. Adsorption study

3.2.1. Influence of time

The influenced of time for adsorption of AB 25 by the NFO-GO and NFO was performed at room temperature (303 K) and depicted in Fig. 8a. This adsorption parameter was investigated for three different experimental sets up and the results obtained with the error bars are explained in Fig. 8b.

In the case of NFO, the maximum q_e value found to be 2.381 mg g^{-1} (240 min). The adsorption process attained an equilibrium within 240 min. The maximum adsorption occurred during the onset of the adsorption and then slowed down by attaining an equilibrium within 240 min. The maximum adsorption at initial periods might be due to the more number of available active sites present in the adsorbent, which facilitated the dye molecule to attach the adsorbent efficiently. With the passes of time, the number of available active sites declined and the process attained equilibrium [35,36].

3.2.2. Influence of pH on AB 25

The pH of the solution is one of the important parameters of any adsorption process. Adsorption of AB 25 preferred at

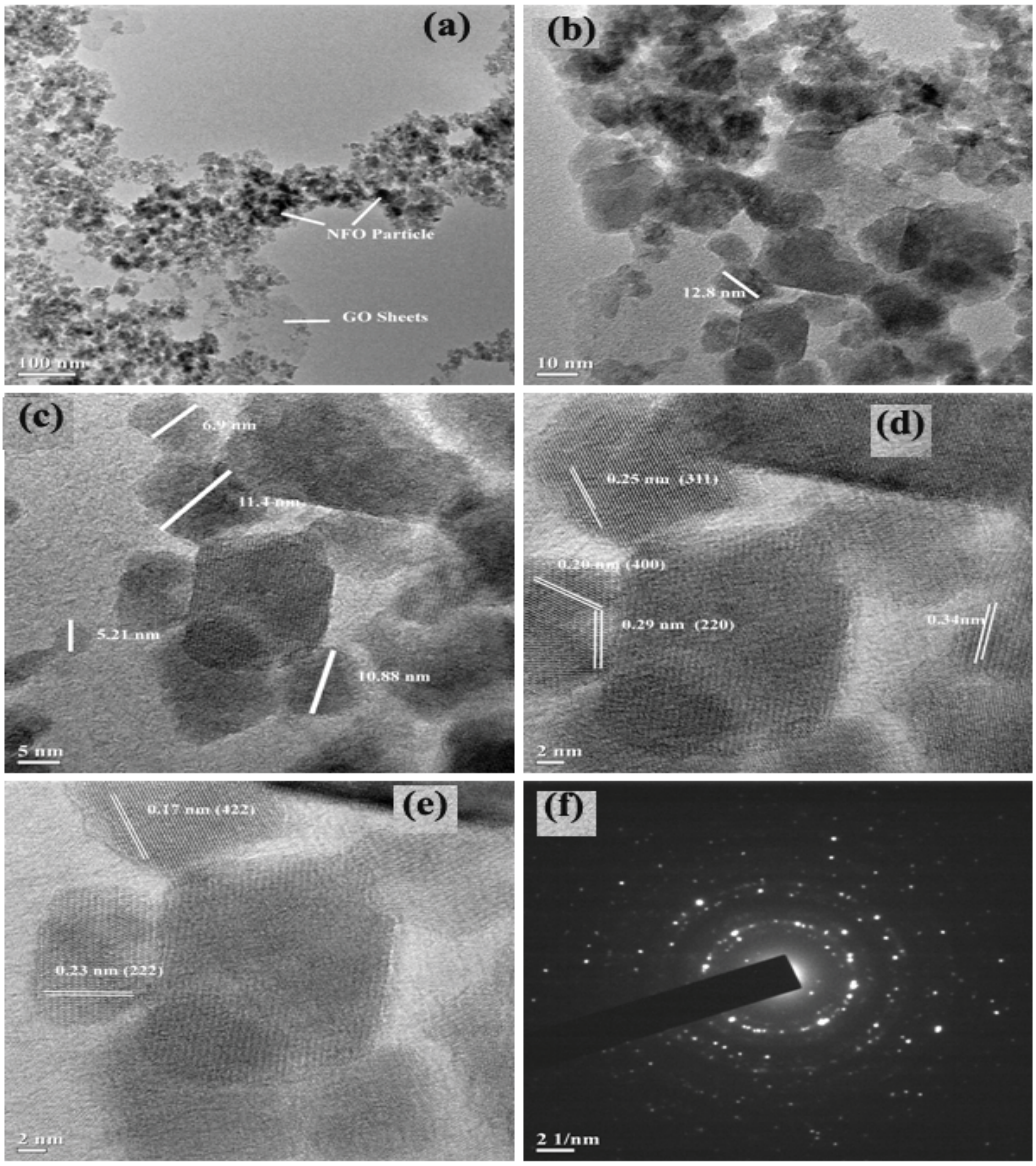

Fig. 3. HRTEM images of $NiFe_2O_4$-graphene oxide composite (a) $NiFe_2O_4$ particle on GO sheet, (b,c) particle size distribution, (d,e) different plane of crystal, and (f) diffraction image of $NiFe_2O_4$-graphene oxide composite.

lower pH [37]. At this stage, more H^+ ions were available in the solution, which might be attracted by the partial negatively charge of the adsorbate and developed the permanent positive site at the adsorbate molecule. Hence, it was observed that the dye molecule more easily attracted by the negative surface (suggested by Zeta potential measurement) of the adsorbent. However, at higher pH, the partial positive site of adsorbate molecule attacked by the OH^- ion in the solution, which diminishing the positive character and hence decreased its affinity towards adsorbent sites, yielding lower adsorption (Fig. 9).

3.2.3. Influence of initial AB 25 concentration

The adsorption of AB 25 per unit mass of adsorbent increased from 86.89 to 97.30 mg g^{-1} by increasing the dye concentration from 10 to 30 mg L^{-1} (Fig. S1). By increasing the dye concentration, the higher driving force provided to overcome the mass transfer resistance of dye between the aqueous phase and the solid phase, resulting in more collision between the dye molecule and solid phase of the adsorbent. At high dye concentration, the unit mass of the adsorbents exposed to a larger number of dye species and progressively higher numbers of dyes taken up with the gradual filling up of the appropriate binding sites. This increased the q_e although the net adsorption comes down [38].

3.2.4. Influence of adsorbent load

Fig. S2 represents the influence of variation of adsorbent load on the removal of AB 25. The amount of dye adsorbed per unit mass of the adsorbent (q_e) decreased from 82.12 to

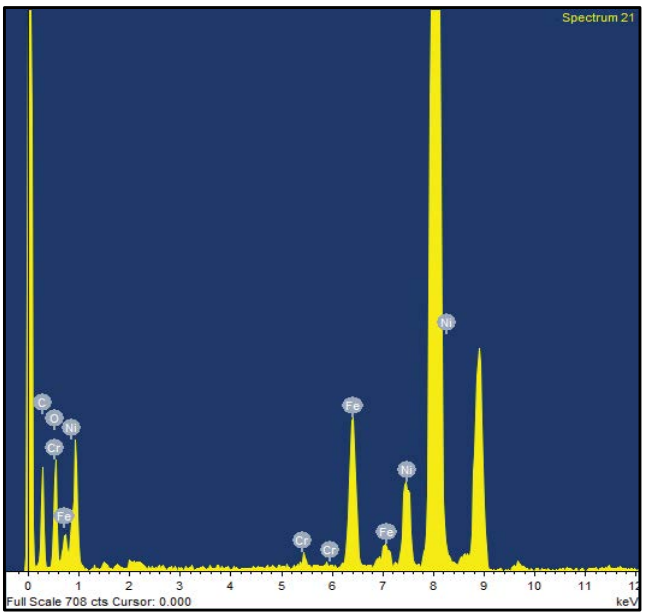

Fig. 4. EDX analysis of $NiFe_2O_4$-graphene oxide composite.

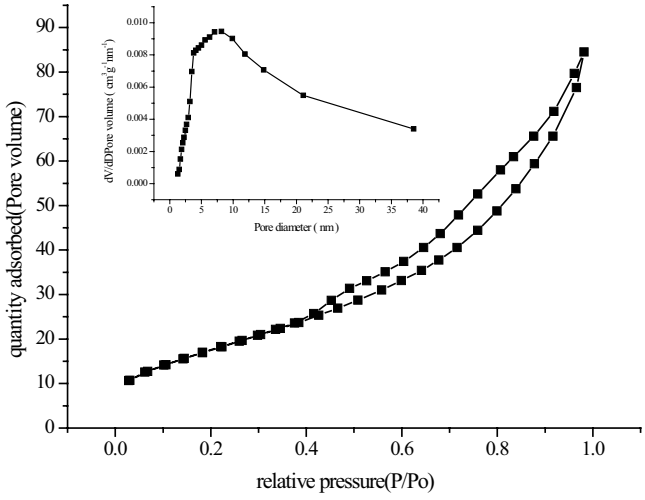

Fig. 5. Nitrogen isotherm and pore size distribution of $NiFe_2O_4$-graphene oxide composite.

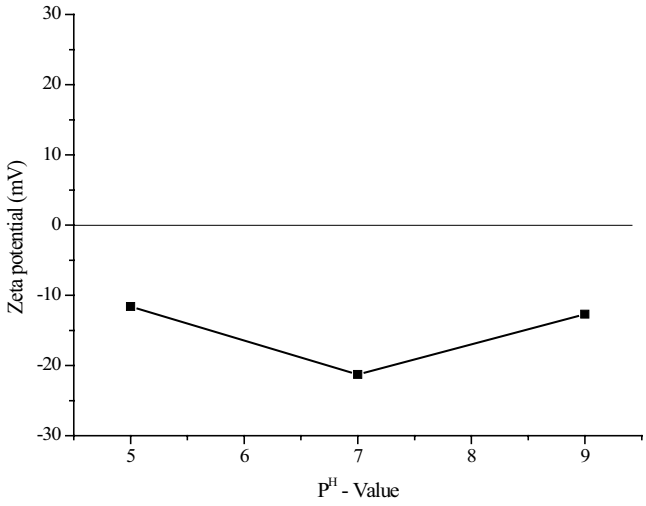

Fig. 6. Zeta potential vs. pH plots of $NiFe_2O_4$-graphene oxide composite.

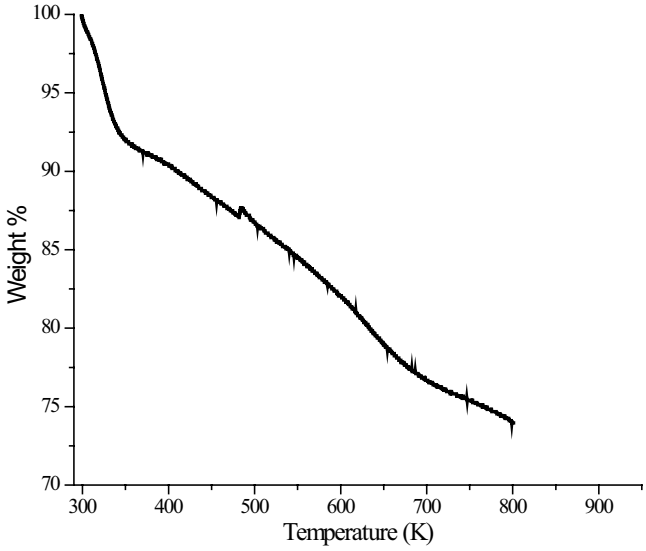

Fig. 7. Thermogravimetric analysis of NFO-GO composite.

55.55 mg g^{-1} by increasing the adsorbent amount from 0.02 to 0.18 g L^{-1}. On the other hand, the extent of adsorption showed a steady increase from 16.12% to 100.0%.

The increase in percentage adsorption might be due to the increase in surface negative charge and a decrease in electrostatic potential near the solid surfaces, which favors adsorbent–adsorbate interaction.

However, the decrease in adsorption density was caused as a large amount of adsorbent effectively reduced the unsaturation of the adsorption sites and correspondingly, the number of such sites per unit mass came down resulting in comparatively less adsorption at the higher adsorbent amount. Furthermore, the dye species could easily access the adsorption sites by a small amount of adsorbent yielding high q_e value. With the rise in adsorbent load, the overcrowding of particles (due to solid concentration-effect) decreased the adsorptive capacity utilization of the adsorbent increase in adsorption per unit mass [39].

3.2.5. Influence of temperature on AB 25

The AB 25 adsorption increased with a rise in temperature from 303 to 333 K showing the endothermic nature of adsorbent-dye interaction (Fig. S3). It may be likely that adsorption of AB 25 on the adsorbent surface requires activation energy and a rise in temperature helps more dye to overcome this energy barrier and get attached to the surface [40,41].

3.2.6. Kinetics study of the adsorption mechanism

Adsorption is a multi-step process involving the transport of solute particles from the liquid phase to the surface of the

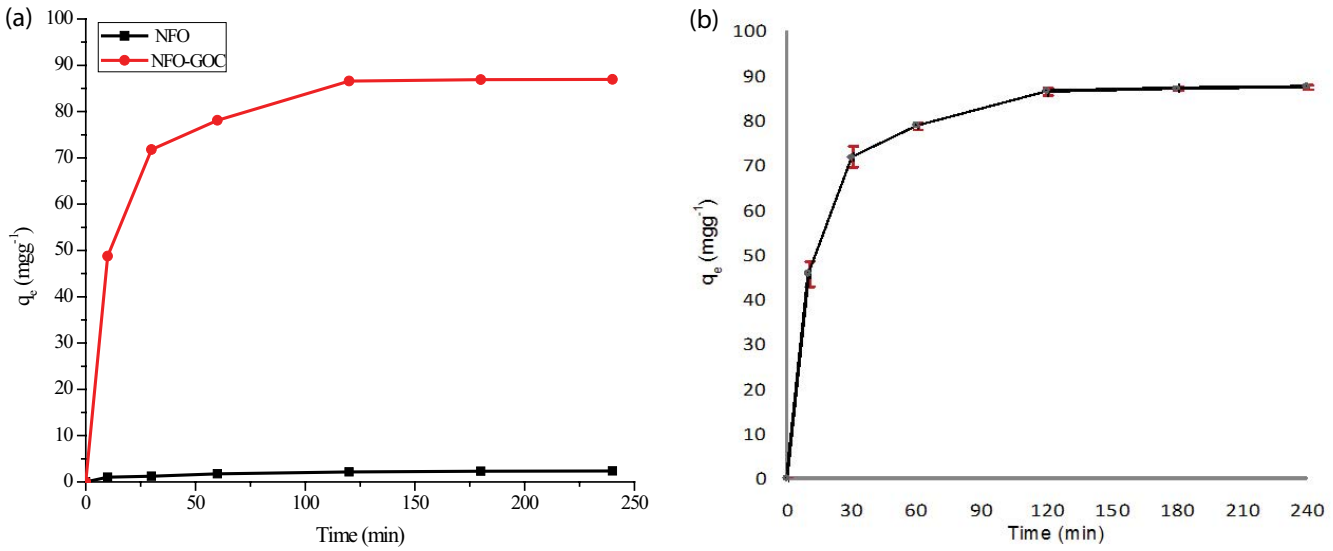

Fig. 8. (a) Influence of time (min) for the adsorption of AB 25 on NFO and NFO-GOC and (b) influence of time (min) for the adsorption of AB 25 on NFO-GOC with error bars.

solid phase of adsorbent followed by diffusion into the interior of the pore that might be a slow process. This idea led to study the kinetics of dye adsorption, by applying the experimental data to various kinetic models, namely, Lagergren pseudo-first-order, second-order, Elovich, intra-particle diffusion, and liquid film diffusion kinetic model.

3.2.6.1. Pseudo-first and second-order kinetics

To understand the kinetics and adsorption mechanism, the pseudo-first-order and pseudo-second-order model were applied by Eqs. (3) and (4) respectively to the adsorption of dye on the NFO-GO composite [42–44]. The equations for the models are:

$$\log\left(q_e - q_t\right) = \log q_e - \frac{K_1 t}{2.303} \tag{3}$$

$$\frac{t}{q_t} = \frac{1}{K_2 q_e^2} + \frac{t}{q_e} \tag{4}$$

where q_e and q_t are dye absorbed (mg g^{-1}) at equilibrium and at any time t (min) in the adsorption process, respectively. K_1 (min^{-1}) and K_2 (g mg^{-1} min^{-1}) were the rate constant for the pseudo-first-order and pseudo-second-order model, respectively. The linear fitting curve of $\log(q_e - q_t)$ vs. t and t/q_t vs. t representing pseudo-first-order (Fig. S4) and pseudo-second-order (Fig. 10) kinetics model, respectively.

It was observed that the calculated q_e value ($q_{e,\text{cal.}}$) obtained from the first-order kinetics model did not agree with the experimental data ($q_{e,\text{exp.}}$) having a deviation of 30.61%. However, the deviation in the case of the second-order model was comparatively less (–3.86%), indicating the proximity of the experimental value to that of a theoretical one. The small deviations obtained in the case might be due to some experimental error. However, the adsorption process was much more akin to the second-order kinetics. The information obtained from the pseudo-second-order model at various temperatures in Table 2.

3.2.6.2. Elovich equation

The Elovich equation [45] was related to the adsorption process by assuming that (i) solid surface is energetically heterogeneous and (ii) neither desorption nor interaction between the adsorbed species could substantially affect the kinetics of adsorption at low surface coverage. The equation can be expressed as:

$$q_t = \left(\frac{1}{\beta}\right)\ln\left(\alpha\beta\right) + \left(\frac{1}{\beta}\right)\ln t \tag{5}$$

The parameter α could be considered as the initial rate at $t = 0$ ($dq_t/dt = \alpha$) and β was the Elovich constant. The linearity of the q_t vs. ln$t$ plots (Eq. (5)) shows good agreement for accurate measurement of the kinetics parameter of the Elovich equation. The suggested values from the plots for the correlation coefficient, the constant α (adsorption coefficient) and β (desorption coefficient) were $R = 0.946$ (low), 9.52 mg g^{-1} min^{-1} and 8.4 × 10^{-2} g mg^{-1}, respectively.

3.2.6.3. Intra-particle diffusion

In the case of porous adsorbent, the diffusion of adsorbates molecules or ions into the pores of adsorbent cannot deny. Thus, it was also taken into account to find out the suitable kinetic model for the adsorption process. The intra-particle diffusion model was simplified by Weber and Morris [46,47] as expressed by:

$$q_t = k_i t^{0.5} + C \tag{6}$$

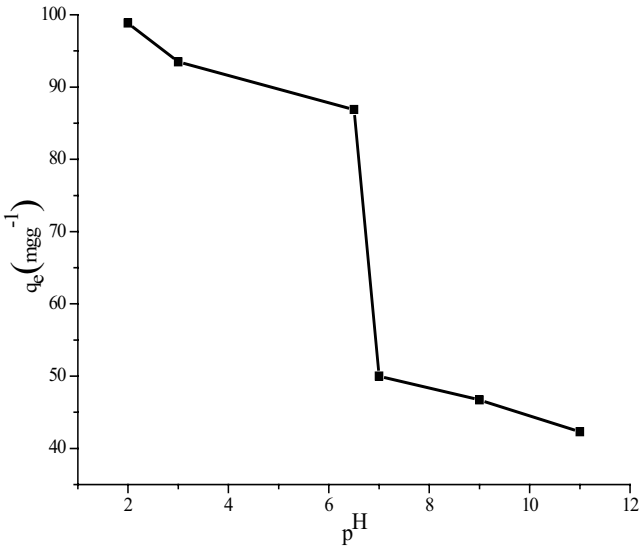

Fig. 9. Influence of pH for adsorption of AB 25 on NFO-GOC.

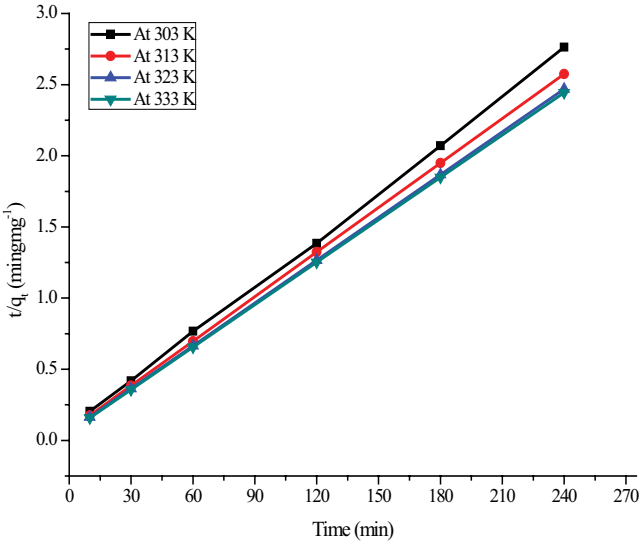

Fig. 10. Pseudo-second-order plots for AB 25 adsorption on NFO-GOC.

where k_i (mg g^{-1} min$^{0.5}$) was the rate parameter for intra-particle diffusions. The data obtained were k_i (2.75 mg g^{-1} min$^{0.5}$) the rate parameter at stage *i*, constant *C* could be calculated from the linearity of the plots q_t vs. $t^{0.5}$ (Eq. (6)) and interpreted as boundary layer effect. The high values of intercept (50.73 mg g^{-1}) suggested that the intra-particle diffusion might not play any significant role in the overall dye adsorption process.

3.2.6.4. Liquid film diffusion

The liquid film mass transfer rate equation was represented [48] by Eq. (7):

$$-\ln\left(1-\frac{q_t}{q_e}\right)=K_d t \tag{7}$$

where K_d (min^{-1}) is the rate parameter for liquid film diffusions. The linear fitting plots of Eq. (7) (Fig. S5) revealed that the liquid film diffusion process followed partially in the adsorption with intercept + 0.36 and liquid film diffusion constant 0.04 min^{-1}, indicating that the liquid film diffusion might play some roles in the overall dye adsorption mechanism.

3.2.7. Adsorption isotherm

Adsorption allows the accumulation of chemical species into the solid phase of the adsorbent and interfaces between them. The empirical isotherm models provide information about the experimental finding. The different isotherm models applied to describe an adsorption process are Langmuir/Freundlich, Temkin, and Dubinin–Radushkevich (D-R) isotherm model.

3.2.7.1. Langmuir and Freundlich isotherm

The adsorption isotherm for the adsorption of dye on NFO-GO composite at room temperature investigated for Langmuir [49] and Freundlich [50] isotherm. The linear form of Langmuir [51] and Freundlich [52] equation expressed by Eqs. (8) and (9), respectively.

Table 2
Kinetic parameters for the AB adsorption

Pseudo-first-order kinetics					
C_0 (mgL^{-1})	K_1 (min^{-1})	$q_{e,cal.}$ (mg g^{-1})	$q_{e,exp.}$ (mg g^{-1})	Deviation (%)	*R*
10	3.98 × 10^{-2}	60.29	86.89	30.61%	–0.983
Pseudo-second-order kinetics					
C_0 (mgL^{-1})	Temperature (K)	K_2 (g mg^{-1} min^{-1})	$q_{e,cal.}$ (mg g^{-1})	$q_{e,exp.}$ (mg g^{-1})	Deviation (%)	*R*
10	303	1.41 × 10^{-3}	90.25	86.89	–3.86%	+0.999
	313	1.52 × 10^{-3}	95.88	93.21	–2.86%	
	323	1.58 × 10^{-3}	99.8	97.23	–2.64%	
	333	1.69 × 10^{-3}	100.6	98.19	–2.45%	

$$\frac{C_e}{q_e} = \frac{C_e}{q_m} + \frac{1}{bq_m} \tag{8}$$

$$\log\left(q_e\right) = \log k_f + \frac{\log\left(C_e\right)}{n} \tag{9}$$

where C_e (mg L^{-1}) is the equilibrium concentration of the dye solution, q_e (mg g^{-1}) is equilibrium adsorption capacity, q_m (mg g^{-1}) is the Langmuir theoretical saturation adsorption capacity and b is Langmuir constant. In the Freundlich equation, the k_f ($mg^{1-1/n}\,L^{1/n}\,g^{-1}$) is the binding energy constant reflecting the affinity of adsorbent to dye molecule and n is the Freundlich constant.

The linear fitting curves (i) C_e/q_e vs. C_e and (ii) $\log q_e$ vs. $\log C_e$ of dye adsorption for the Langmuir and Freundlich isotherm model were plotted. The isotherm values along with the correlation coefficients listed in Table 3. The experimental value fitted better with the Langmuir isotherm model (Fig. 11) then the Freundlich isotherm model (Fig. S6). The Langmuir adsorption monolayer capacity calculated was 104.16 mg g^{-1} for AB 25.

3.2.7.2. Temkin isotherm study

Temkin assumes that due to adsorbent–adsorbate interaction the heat of adsorption of all molecules decreases linearly with coverage. The adsorption process could be characterized by uniform binding energy up to maximum binding energy [53]. Temkin Isotherm could be applied in the adsorption process as described in the linear form [54] by Eq. (10).

$$q_e = \frac{2.303RT}{b_T}\left(\log A_T + \log C_e\right) \tag{10}$$

where $RT/b_T = B$ (J mol^{-1}) is the Temkin constant corresponds to sorption, A_T (g^{-1}) was the equilibrium binding constant corresponding to maximum binding energy, R ($JK^{-1}\,mol^{-1}$) is the gas constant and T is the temperature of the solution in Kelvin (K).

The information obtained from the linear fitting q_e vs. $\log C_e$ curve for Temkin isotherm showed correlation co-efficient value, R = 0.949 that appreciated the monolayer adsorption of AB 25 on NFO-GO.

3.2.7.3. D-R isotherm model

The D-R isotherm [55] equation with its numerous modifications plays an important role in the adsorption process characteristics of porous adsorbent with a wide range of pore size and shape [56]. The linear form of the D-R isotherm equation and the energy equation for desorption are depicted in Eqs. (11) [57] and (12), respectively.

$$\ln q_e = \ln q_s - K_{dr}\varepsilon^2 \tag{11}$$

$$E = \left(2K_{dr}\right)^{-0.5} \tag{12}$$

Table 3
The correlation coefficient for the adsorption isotherm of Acid blue 25 adsorption

Langmuir isotherm		
b	q_m (mg g^{-1})	R
0.12	104.16	0.999
Freundlich isotherm		
n	k_f ($mg^{1-1/n}\,L^{1/n}\,g^{-1}$)	R
11.79	70.79	0.952
Temkin isotherm		
A_T (g^{-1})	B (J mol^{-1})	R
1,151.97	9.437	0.949
Dubinin–Raduschkevich Isotherm		
q_s (mgg^{-1})	E (kJ mol^{-1})	R
95.63	3.12	0.875

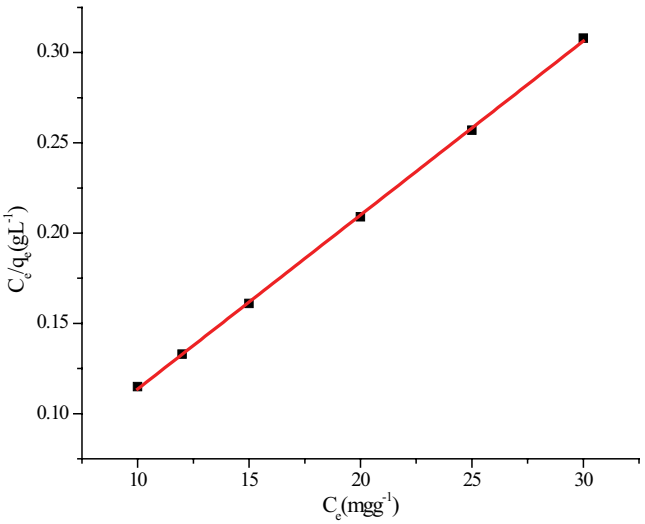

Fig. 11. Langmuir isotherm model for AB 25 adsorption on NFO-GOC.

where q_s (mg g^{-1}) is the D-R theoretical saturation capacity, K_{dr} (mol^2/J^2) is D-R isotherm constant related to free energy, ε is the Polanyi potential, defined as $\varepsilon = RT\ln(1 + 1/C_e)$ and E (kJ mol^{-1}) is the energy per molecule of the adsorbate for removing a molecule from its location at the sorption site to infinity.

The values of the parameter (Table 3) from the linear fitting $\ln q_e$ vs. ε^2 curve (Fig. 12) for D-R isotherm are q_s = 95.63 mg g^{-1} and E = 3.12 kJ mol^{-1}. This suggested the physical adsorption of AB 25 on the adsorbent.

The comparison of Langmuir monolayer capacity of various adsorbent for the adsorption of AB 25 listed in Table 4.

3.3. Thermodynamic study

The thermodynamics parameter ΔH, ΔS, ΔG for the adsorption process of dye on the adsorbent were computed by the equation.

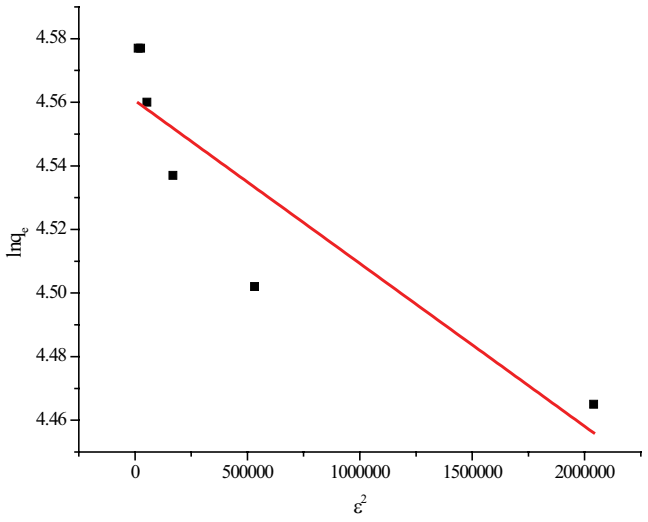

Fig. 12. Dubinin–Radushkevich isotherm model for AB 25 adsorption on NFO-GOC.

$$\ln K_d = \frac{\Delta S}{R} - \frac{\Delta H}{RT} \tag{13}$$

$$\Delta G = \Delta H - T\Delta S \tag{14}$$

where K_d (q_e/C_e) is the distribution coefficient calculated from experiment, T is the temperature in Kelvin scale (K), R is the ideal gas constant (8.314 JK^{-1} mol^{-1}), ΔS stands for the entropy change during the adsorption process, ΔH is the change in enthalpy and ΔG is Gibb's free energy change.

To calculate the activation energy of adsorption, the Arrhenius equation had been applied by using the equation given below.

$$\log K_2 = \log A - \frac{E_a}{2.303RT} \tag{15}$$

where K_2 (g mg^{-1} min^{-1}) is the pseudo-second-order rate constant obtained from the kinetic model, E_a (kJ mol^{-1}) is Arrhenius activation energy for adsorption and A is the Arrhenius factor.

The value for the ΔS and ΔH calculated from the intercept and slope of the plot of the linear fitting $\ln K_d$ vs. $1/T$ of Eq. (13) and the value of ΔG calculated from Eq. (14). All the thermodynamic values are listed in Table 5. The endothermic adsorbate–adsorbent interaction suggested by the positive value of ΔH. The positive value of ΔS indicated the rise in randomness at a solid-solution interface that might be due to some structural change of adsorbate and adsorbent in the adsorption process. The negative Gibb's free energy (ΔG) for the adsorption process increased with a rise in temperature also indicated the spontaneity of both the dye adsorption process.

Table 4
Comparison of Langmuir monolayer capacity for AB from literature

Adsorbent	Langmuir monolayer capacity q_m (mg g^{-1})	References
Hazelnut	60.2	[36]
Peat	14.4	[58]
Diatomite	21.41	[59]
NFO-GO	104.16	This work

The Arrhenius parameter was determined by the linear fitting curve of $\log K_2$ vs. $1/T$ of Eq. (15) provided the slope of $-E_a/2.303R$ and the intercept of $\log A$ (Fig. 13). The result obtained for activation energy was 4.87 kJ mol^{-1} indicated that the adsorption process might be physically controlled [60].

3.4. Reusability study

The reusability of NFO-GOC was examined by performing several adsorption and desorption in the ethanol/acetic acid solution cycle (Fig. 14). In each cycle, the adsorbed AB 25 dye was desorbed from ethanolic/acetic acid solution after stirring about 12 h by magnetic stirrer at room temperature. After the first cycle of adsorption-desorption from ethanolic/acetic acid solution, 97.9% of the adsorption capacity of NFO-GOC was recovered. After the 3rd cycle, the adsorption ability of NFO-GOC was retained at 91.09% of the original value. However, without desorption, the adsorption capacity of the adsorbent decreased down to 58.88% after the first cycle which further decreased down to 20.8% of the original value after the 3rd cycle. Therefore, the desorption by ethanol/acetic acid solution was effective to recover the adsorption efficiency of NFO-GOC.

4. Conclusion

The adsorption of AB 25 dye was studied using NFO-GOC. The results of the study summarized as follows:

- The adsorbent NFO-GO was successfully prepared and the characterization study suggested that the composite was in the nano range.
- The dye removal process preferably followed the Langmuir isotherm with the monolayer adsorption capacities 104.16 mg g^{-1}.

Table 5
Thermodynamic data for dye adsorption

Dye	ΔH (kJ mol^{-1})	ΔS (JK^{-1} mol^{-1})	E_a (kJ mol^{-1})	ΔG (kJ K^{-1} mol^{-1})			
				303 K	313 K	323 K	333 K
AB	+64.319	+248.84	4.87	–11.1	–13.56	–16.1	–18.54

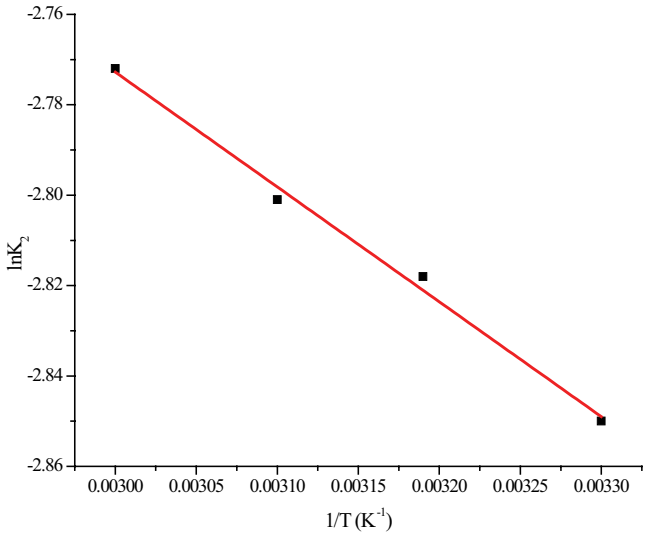

Fig. 13. Arrhenius plots for AB 25 adsorption on NFO-GOC.

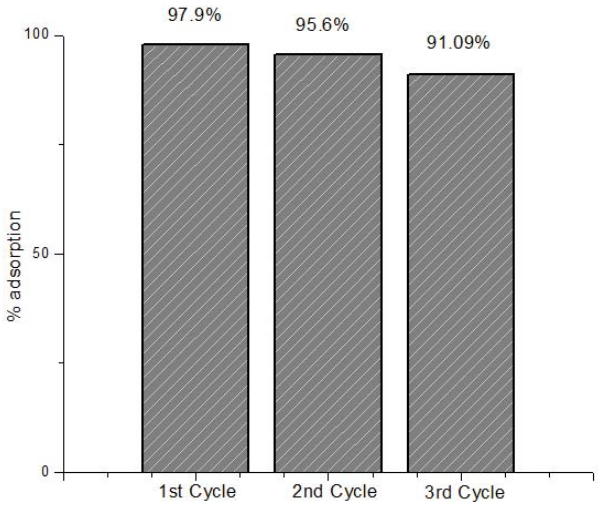

Fig. 14. Reusability of NFO-GOC on successive use for adsorption of AB 25.

- The adsorption process obeyed the second-order kinetics model.
- The dye adsorptions were endothermic.
- The NFO-GO-dye interactions were spontaneous and governed by a decreased in Gibb's free energy.
- The dye adsorptions were pH-sensitive.
- The reusability study indicated that the adsorption capacity of NFO-GOC was retained at 91.09% of the original value even after the 3rd adsorption–desorption cycle.

Acknowledgments

The authors are thankful to NEHU, shilling, IITG, Guwahati and USIC, Gauhati University, IIAST for measuring transmission electron microscopy, XRD and Zeta potential respectively. We are also grateful to the department of chemistry, B N College, Dhubri for allowing us to carry out the experimental work.

References

[1] G. Crini, Recent developments in polysaccharide-based materials used as adsorbents in wastewater treatment, Prog. Polym. Sci., 30 (2005) 38–70.
[2] W.J. Weber Jr., P.M. McGinley, L.E. Katz, Sorption phenomena in subsurface systems: concepts, models and effects on contaminant fate and transport, Water Res., 25 (1991) 499–528.
[3] N. Bektaş, S. Kara, Removal of lead from aqueous solutions by natural clinoptilolite: equilibrium and kinetic studies, Sep. Purif. Technol., 39 (2004) 189–200.
[4] L. Lian, L.P. Guo, C.J. Guo, Adsorption of Congo red from aqueous solutions onto Ca-bentonite, J. Hazard. Mater., 161 (2009) 126–131.
[5] S.T. Akar, R. Uysal, Untreated clay with high adsorption capacity for effective removal of C.I. Acid Red 88 from aqueous solutions: batch and dynamic flow mode studies, Chem. Eng. J., 162 (2010) 591–598.
[6] L.A. Rodrigues, L.J. Maschio, R.E. da Silva, M.L.C.P. da Silva, Adsorption of Cr(VI) from aqueous solution by hydrous zirconium oxide, J. Hazard. Mater., 173 (2010) 630–636.
[7] M.D. Stoller, S.Y. Park, Y.W. Zhu, J.H. An, R.S. Ruoff, Graphene-based ultracapacitors, Nano Lett., 8 (2008) 3498–3502.
[8] Z. Jin, D. Nackashi, W. Lu, C. Kittrell, J.M. Tour, Decoration, migration, and aggregation of palladium nanoparticles on graphene sheets, Chem. Mater., 22 (2010) 5695–5699.
[9] S. Bai, X.P. Shen, G.X. Zhu, A.H. Yuan, J. Zhang, Z.Y. Ji, D.Z. Qiu, The influence of wrinkling in reduced graphene oxide on their adsorption and catalytic properties, Carbon, 60 (2013) 157–168.
[10] R. Dubey, J. Bajpai, A.K. Bajpai, Green synthesis of graphene sand composite (GSC) as novel adsorbent for efficient removal of Cr (VI) ions from aqueous solution, J. Water Process Eng., 5 (2015) 83–94.
[11] X.K. Wang, C.L. Chen, W.P. Hu, A.P. Ding, D.S. Xu, X.P. Zhou, Sorption of 243Am(III) to multiwall carbon nanotubes, Environ. Sci. Technol., 39 (2005) 2856–2860.
[12] J. Deng, Y.S. Shao, N.Y. Gao, Y. Deng, C.Q. Tan, S.Q. Zhou, X.H. Hu, Multiwalled carbon nanotubes as adsorbents for removal of herbicide diuron from aqueous solution, Chem. Eng. J., 193 (2012) 339–347.
[13] Y.S. Fu, H.Q. Chen, X.Q. Sun, X. Wang, Combination of cobalt ferrite and graphene: high-performance and recyclable visible-light photocatalysis, Appl. Catal., B, 111 (2012) 280–287.
[14] M.J. McAllister, J.-L. Li, D.H. Adamson, H.C. Schniepp, A.A. Abdala, J. Liu, M. Herrera-Alonso, D.L. Milius, R. Car, R.K. Prud'homme, I.A. Aksay, Single sheet functionalized graphene by oxidation and thermal expansion of graphite, Chem. Mater., 19 (2007) 4396–4404.
[15] H. Xia, D.D. Zhu, Y.S. Fu, X. Wang, $CoFe_2O_4$-graphene nanocomposite as a high-capacity anode material for lithium-ion batteries, Electrochim. Acta, 83 (2012) 166–174.
[16] C.X. Guo, H.B. Yang, Z.M. Sheng, Z.S. Lu, Q.L. Song, C.M. Li, Layered graphene/quantum dots for photovoltaic devices, Angew. Chem. Int. Ed., 49 (2010) 3014–3017.
[17] H.L. Wang, H.S. Casalongue, Y.Y. Liang, H.J. Dai, $Ni(OH)_2$ nanoplates grown on graphene as advanced electrochemical pseudocapacitor materials, J. Am. Chem. Soc., 132 (2010) 7472–7477.
[18] Q. Song, Z.J. Zhang, Shape control and associated magnetic properties of spinel cobalt ferrite nanocrystals, J. Am. Chem. Soc., 126 (2004) 6164–6168.
[19] B. Baruwati, M.N. Nadagouda, R.S. Varma, Bulk synthesis of monodisperse ferrite nanoparticles at water-organic interfaces under conventional and microwave hydrothermal treatment and their surface functionalization, J. Phys. Chem. C, 112 (2008) 18399–18404.
[20] Y. Kinemuchi, K. Ishizaka, H. Suematsu, W.H. Jiang, K.S. Yatsui, Magnetic properties of nanosize $NiFe_2O_4$ particles

synthesized by pulsed wire discharge, Thin Solid Films, 407 (2002) 109–113.
[21] H.Y. Guo, T.F. Jiao, Q.R. Zhang, W.F. Guo, Q.M. Peng, X.H. Yan, Preparation of graphene oxide-based hydrogels as efficient dye adsorbents for wastewater treatment, Nanoscale Res. Lett., 10 (2015) 272.
[22] C. Wang, C. Feng, Y.J. Gao, X.X. Ma, Q.H. Wu, Z. Wang, Preparation of a graphene-based magnetic nanocomposite for the removal of an organic dye from aqueous solution, Chem. Eng. J., 173 (2011) 92–97.
[23] J.N. Tiwari, K. Mahesh, N.H. Le, K.C. Kemp, R. Timilsina, R.N. Tiwari, K.S. Kim, Reduced graphene oxide-based hydrogels for the efficient capture of dye pollutants from aqueous solutions, Carbon, 56 (2013) 173–182.
[24] X.M. Wang, M.X. Lu, H. Wang, Y.F. Pei, H.H. Rao, X.Z. Du, Three-dimensional graphene aerogels–mesoporous silica frameworks for superior adsorption capability of phenols, Sep. Purif. Technol., 53 (2015) 7–13.
[25] K. Lu, G.X. Zhao, X.K. Wang, A brief review of graphene-based material synthesis and its application in environmental pollution management, Chin. Sci. Bull., 57 (2012) 1223–1234.
[26] J.F. Wang, T. Tsuzuki, B. Tang, X.L. Hou, L. Sun, X.G. Wang, Reduced graphene oxide/ZnO composite: reusable adsorbent for pollutant management, ACS Appl. Mater. Interfaces, 4 (2012) 3084–3090.
[27] G.Q. Xie, P.X. Xi, H.Y. Liu, F.J. Chen, L. Huang, Y.J. Shi, F.P. Hou, Z.Z. Zeng, C.W. Shao, J. Wang, A facile chemical method to produce superparamagnetic graphene oxide–Fe_3O_4 hybrid composite and its application in the removal of dyes from aqueous solution, J. Mater. Chem., 22 (2012) 1033–1039.
[28] W.S. Hummers Jr., R.E. Offeman, Preparation of graphitic oxide, J. Am. Chem. Soc., 80 (1958) 1339–1339.
[29] D.C. Marcano, D.V. Kosynkin, J.M. Berlin, A. Sinitskii, Z.Z. Sun, A. Slesarev, L.B. Alemany, W. Lu, J.M. Tour, Improved synthesis of graphene oxide, ACS Nano, 4 (2010) 4806–4814.
[30] D. Caruntu, Y. Remond, N.H. Chou, M.-J. Jun, G. Caruntu, J.B. He, G. Goloverda, C. O'Connor, V. Kolesnichenko, Reactivity of 3d transition metal cations in diethylene glycol solutions. Synthesis of transition metal ferrites with the structure of discrete nanoparticles complexed with long-chain carboxylate anions, Inorg. Chem., 41 (2002) 6137–6146.
[31] S. Bai, X.P. Shen, X. Zhong, Y. Liu, G.X. Zhu, X. Xu, K.M. Chen, One-pot solvothermal preparation of magnetic reduced graphene oxide-ferrite hybrids for organic dye removal, Carbon, 50 (2012) 2337–2346.
[32] B.D. Cullity, S.R. Stock, Elements of X-ray diffraction, 3rd ed., Prentice-Hall, New York, 2001.
[33] G.D. Chen, M. Sun, Q. Wei, Y.F. Zhang, B.C. Zhu, B. Du, Ag_3PO_4/graphene-oxide composite with remarkably enhanced visible-light-driven photocatalytic activity toward dyes in water, J. Hazard. Mater., 244 (2013) 86–93.
[34] L.C.A. Oliveira, R.V.R.A. Rios, J.D. Fabris, V. Garg, K. Sapag, R.M. Lago, Activated carbon/iron oxide magnetic composites for the adsorption of contaminants in water, Carbon, 40 (2002) 2177–2183.
[35] A.S. Özcan, B. Erdem, A. Özcan, Adsorption of Acid Blue 193 from aqueous solutions onto Na–bentonite and DTMA–bentonite, J. Colloid Interface Sci., 280 (2004) 44–54.
[36] F. Ferrero, Dye removal by low cost adsorbents: hazelnut shells in comparison with wood sawdust, J. Hazard. Mater., 142 (2007) 144–152.
[37] I.M. Lipatova, L.I. Makarova, A.A. Yusova, Adsorption removal of anionic dyes from aqueous solutions by chitosan nanoparticles deposited on the fibrous carrier, Chemosphere, 212 (2018) 1155–1162.
[38] K.G. Bhattacharyya, S. Sen Gupta, Adsorption of Co(II) from aqueous medium on natural and acid activated kaolinite and montmorillonite, Sep. Sci. Technol., 42 (2007) 3391–3418.
[39] N.A. Oladoja, A.K. Akinlabi, Congo red biosorption on palm kernel seed coat, Ind. Eng. Chem. Res., 48 (2009) 6188–6196.
[40] A. Shukla, Y.-H. Zhang, P. Dubey, J.L. Margrave, S.S. Shukla, The role of sawdust in the removal of unwanted materials from water, J. Hazard. Mater., 95 (2002) 137–152.
[41] S. Sen Gupta, K.G. Bhattacharyya, Removal of Cd(II) from aqueous solution by kaolinite, montmorillonite and their poly(oxo zirconium) and tetrabutylammonium derivatives, J. Hazard. Mater. B, 128 (2006) 247–257.
[42] S. Lagergren, Zurtheorie der sogenannten adsorption gel osterstoffe, Kungliga Svenska Vetenskaps akademiens Handlingar, 24 (1898) 1–39.
[43] Y.S. Ho, G. McKay, Kinetic models for the sorption of dye from aqueous solution by wood, Process Saf. Environ. Prot., 76 (1998) 183–191.
[44] Y.S. Ho, G. McKay, Pseudo-second-order model for sorption processes, Process Biochem., 34 (1999) 451–465.
[45] S.H. Chien, W.R. Clayton, Application of Elovich equation to the kinetics of phosphate release and sorption in soils, Soil Sci. Soc. Am. J., 44 (1980) 265–268.
[46] W.J. Weber, J.C. Morris, Kinetics of adsorption on carbon from solution, J. Sanitary Eng. Div., 89 (1963) 31–60.
[47] M. Alkan, Ö. Demirbaş, M. Doğan, Adsorption kinetics and thermodynamics of an anionic dye onto sepiolite, Microporous Mesoporous Mater., 101 (2007) 388–396.
[48] G.E. Boyd, A.W. Adamson, L.S. Myers Jr., The exchange adsorption of ions from aqueous solutions by organic zeolites. II. Kinetics, J. Am. Chem. Soc., 69 (1947) 2836–2848.
[49] I. Langmuir, The Constitution and fundamental properties of solids and liquids. Part I. Solids, J. Am. Chem. Soc., 38 (1916) 2221–2295.
[50] H. Freundlich, Uber die adsorption in losungen [Adsorption in solution], Z. Physikalische Chemie, 57 (1906) 385–471.
[51] D.G. Kinniburgh, General purpose adsorption isotherms, Environ. Sci. Technol., 20 (1986) 895–904.
[52] T.T. Chao, M.E. Harward, S.C. Fang, Adsorption and desorption phenomena of sulfate ions in soils, Soil Sci. Soc. Am. Proc., 26 (1962) 234–237.
[53] M.I. Temkin, Kinetics of ammonia synthesis on promoted iron catalysts, Acta Phys. Chim. Sin. URSS, 12 (1940) 327–356.
[54] C.C. Travis, E.L. Etnier, A survey of sorption relationships for reactive solutes in soil, J. Environ. Qual., 10 (1981) 8–17.
[55] O. Redlich, D.L. Peterson, A useful adsorption isotherm, J. Phys. Chem., 63 (1959) 1024–1024.
[56] N.D. Hutson, R.T. Yang, Theoretical basis for the Dubinin–Radushkevitch (D-R) adsorption isotherm equation, Adsorption, 3 (1997) 189–195.
[57] S. Aksoyoglu, Sorption of U(VI) on granite, J. Radioanal. Nucl. Chem. Art., 134 (1989) 393–403.
[58] Y.S. Ho, G. McKay, Sorption of dye from aqueous solution by peat, Chem. Eng. J., 70 (1998) 115–124.
[59] K. Badii, F.D. Ardejani, M.A. Saberi, N.Y. Limaee, S. Zia-e-din Shafaei, Adsorption of Acid blue 25 dye on diatomite in aqueous solutions, Indian J. Chem. Technol., 17 (2010) 7–16.
[60] I.A.W. Tan, A.L. Ahmad, B.H. Hameed, Adsorption isotherms, kinetics, thermodynamics and desorption studies of 2,4,6-trichlorophenol on oil palm empty fruit bunch-based activated carbon, J. Hazard. Mater., 164 (2009) 473–482.

Supplementary information

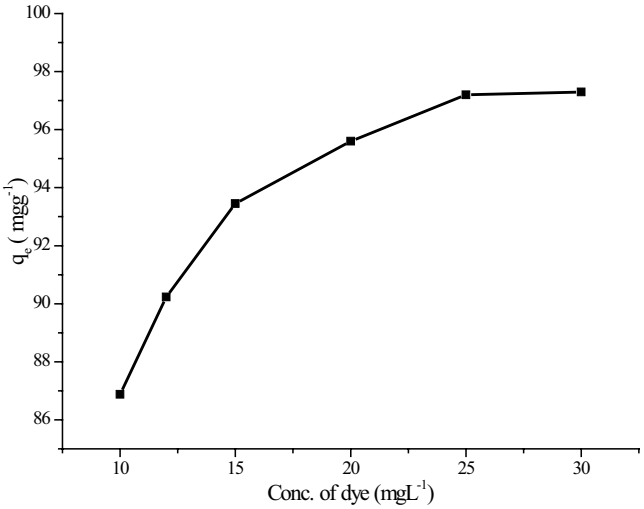

Fig. S1. Influence of initial dye (AB 25) concentration for adsorption on NFO-GOC.

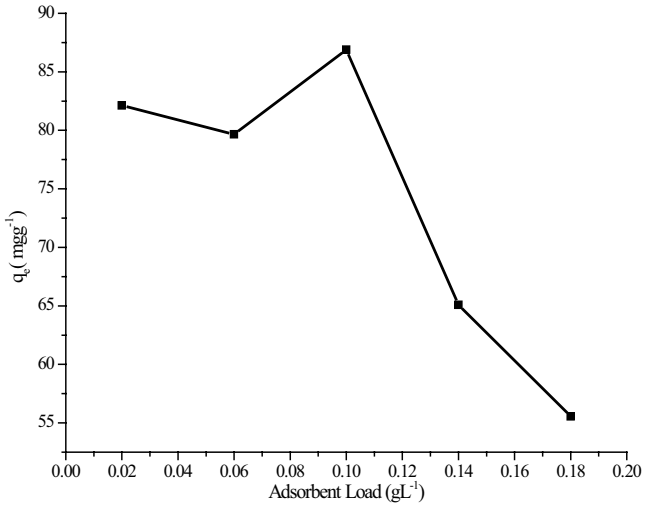

Fig. S2. Influence of adsorbent (NFO-GOC) load for the adsorption of AB 25.

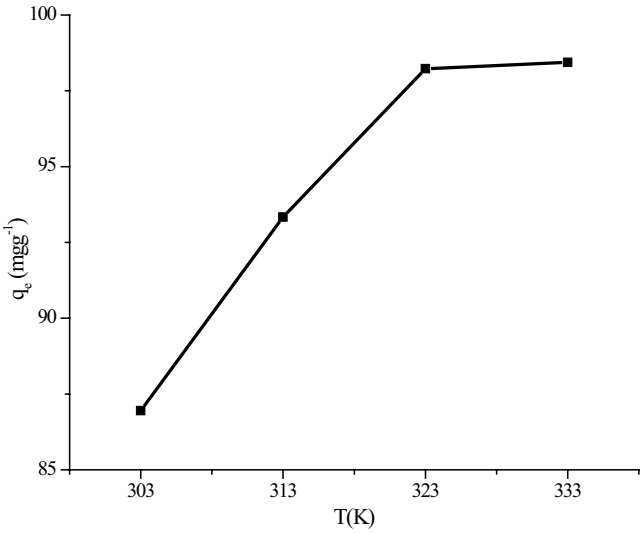

Fig. S3. Influence of temperature for AB 25 adsorption on NFO-GOC.

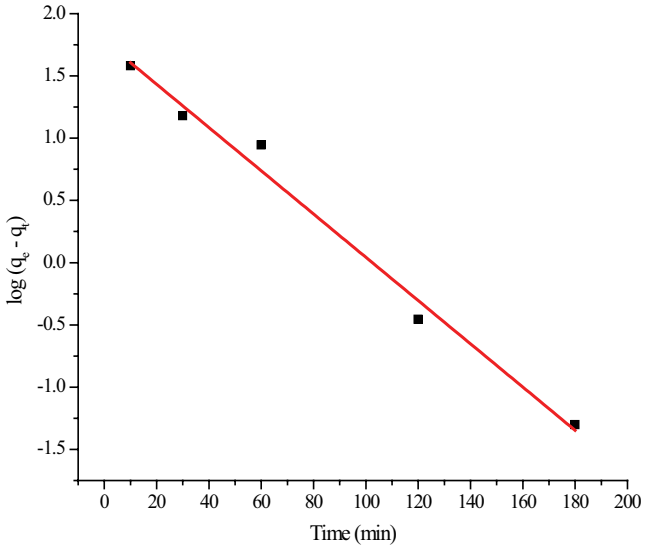

Fig. S4. Pseudo-first-order plots for AB 25 adsorption on NFO-GOC.

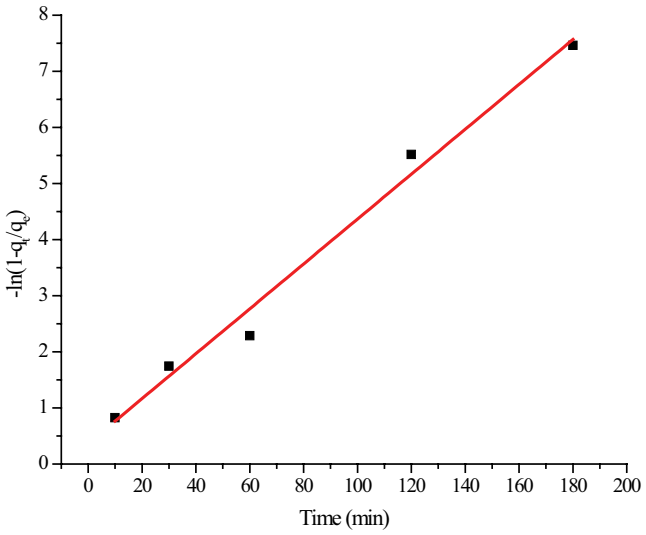

Fig. S5. A liquid film diffusion model for AB 25 adsorption on NFO-GOC.

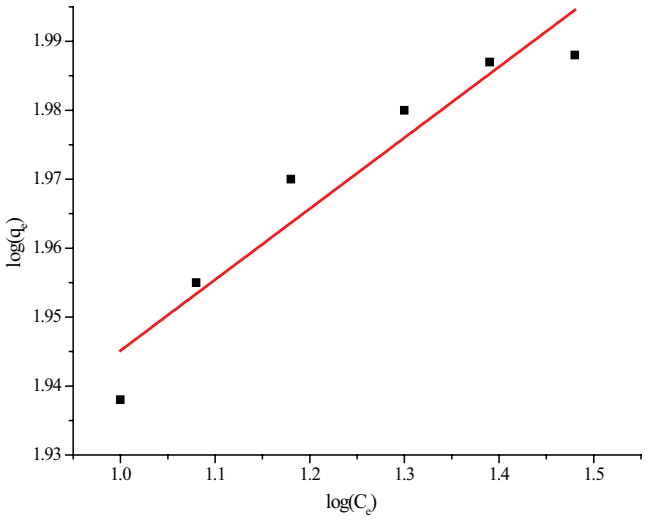

Fig. S6. Freundlich isotherm model for AB 25 adsorption on NFO-GOC.